Electronic Supplementary Material (ESI) for Journal of Materials Chemistry A.
This journal is © The Royal Society of Chemistry 2021

Supporting Information

Sb_2O_3@Sb Nanoparticles Impregnated in N-doped Carbon Microcages for Ultralong Life and High-Rate Sodium Ion Battery

Anding Xu [a], Chuyun Huang [a], Guilan Li [a], Kaixiang Zou [b], Hao Sun [b], Lili Fu [b], Jiahao Ju [b], Yang Song [b], Songping Wu [b, e], Zhiguang Xu* [c], Yurong Yan* [a, d]*

[a] School of Materials Science and Engineering, South China University of Technology, Guangzhou, 510641 (China)

[b] School of Chemistry and Chemical Engineering, South China University of Technology, Guangzhou, 510641 (China)

[c] Key Laboratory of Theoretical Chemistry of Environment, Ministry of Education, School of Chemistry & Environment, South China Normal University, Guangzhou, 510006 (China)

[d] Key Lab of Guangdong High Property & Functional Polymer Materials, Guangzhou 510640 (China)

[e] Guangdong Key Laboratory of Fuel Cell Technology, Guangzhou, 510641 (China)

* Corresponding author, E-mail: chwsp@scut.edu.cn, yryan@scut.edu.cn, chzgxu@scnu.edu.cn

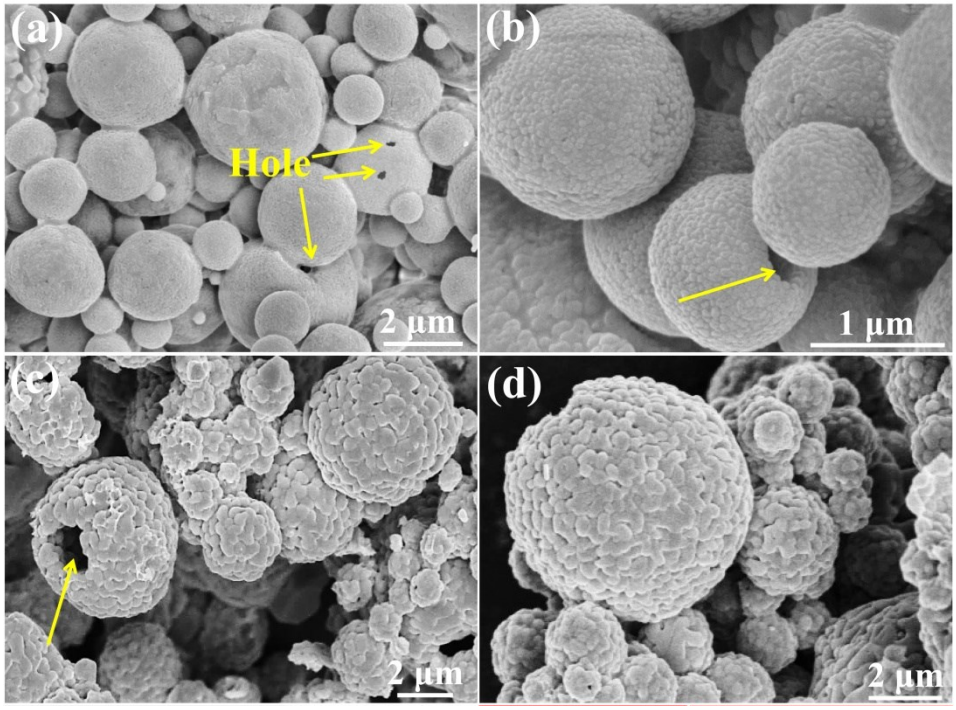

Fig. S1 SEM images of (a-b) the precursor after spray drying; (c-d) the Sb_2O_3@Sb@NC@KCl.

Under the hot air turbulence of spray drying, the Sb_2O_3@Sb@NC precursor displayed a spherical and internally hollow structure (marked by yellow arrows) with a size range of 1-4 μm mostly, which was consisted of numerous KCl nanocubes coated by carbon-containing layer (**Fig. S1a-b**). After annealing, the coating layer on the precursor surface was carbonized and transformed into rugged face (**Fig. S1c-d**). Simultaneously, the Sb source was pyrolyzed and partially reduced to yield Sb_2O_3@Sb heterojunction. Accordingly, the Sb_2O_3@Sb heterojunction was *in-situ* impregnated into N-doping carbon matrix.

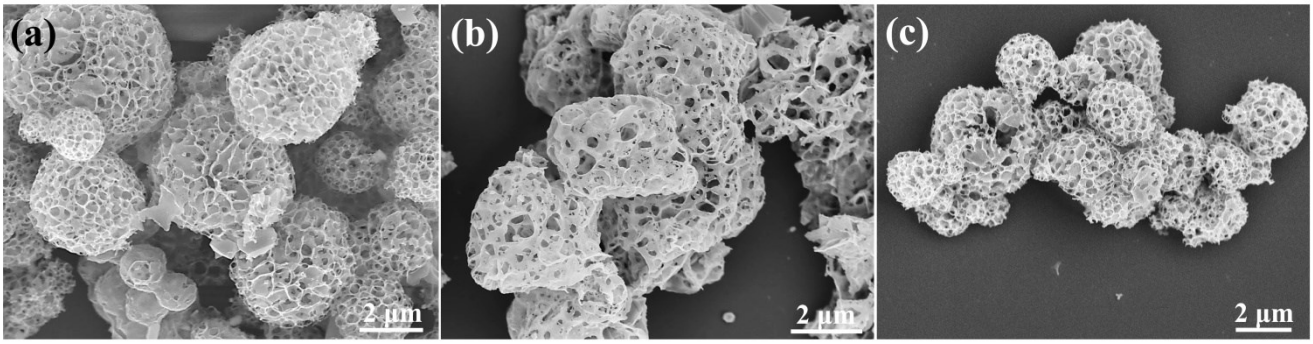

Fig. S2 SEM images of (a) Sb_2O_3@ NC, (b) Sb_2O_3@Sb@C and (c) Sb@NC composites.

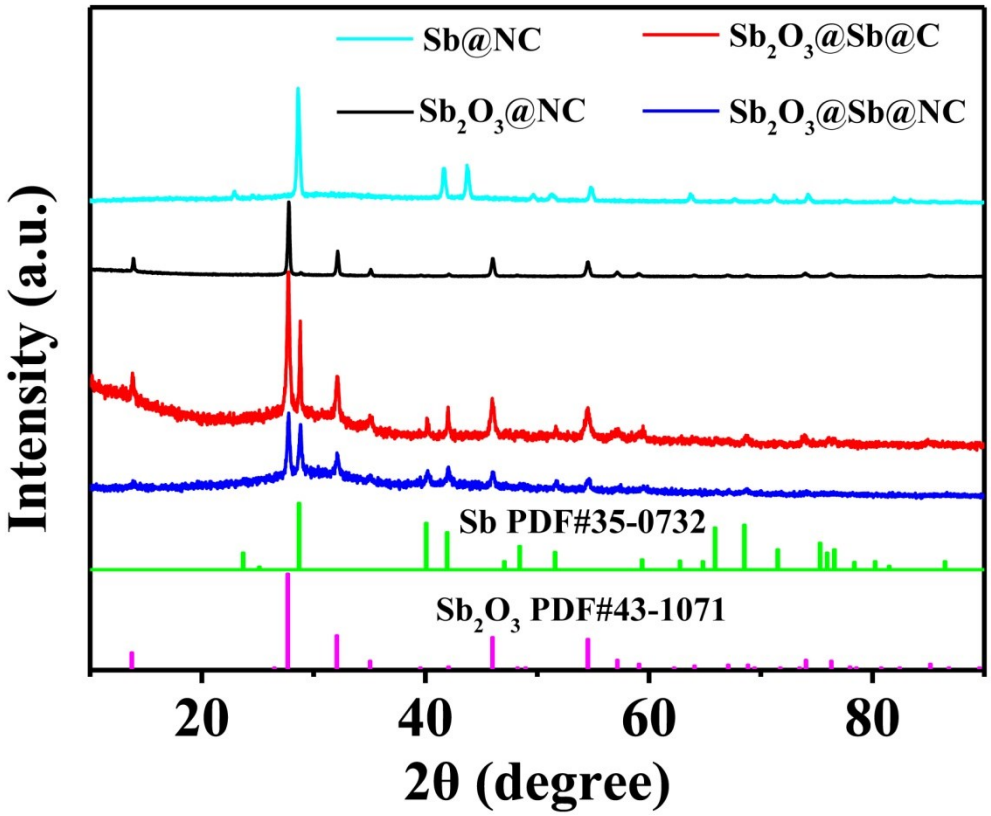

Fig. S3 XRD patterns of Sb_2O_3@NC**,** Sb@NC, Sb_2O_3@Sb@C, and Sb_2O_3@Sb@NC composites.

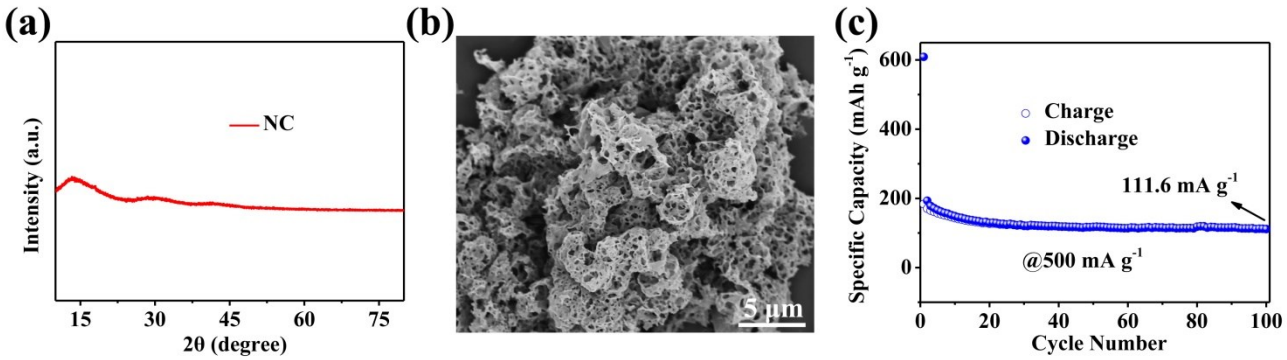

Fig. S4 (a) XRD, (b) SEM and (c) cycling performance of NC.

The XRD indicated its amorphous structure of NC. The NC composites displayed a porous cracked sphere-like structure, which displayed stable capacity of 111.6 mAh g^{-1} under 0.5 A g^{-1}. The theoretical specific capacity of Sb_2O_3@Sb@NC composite could be calculated by the following equation:

$$\text{Specific Capacity} = W_{Sb_2O_3} \times 1103 + W_{Sb} \times 660 + W_{NC} \times 111.6$$

$$= 25.51\% \times 1103 + 20.96\% \times 660 + 53.53\% \times 111.6$$

$$= 479.45 \text{ mAh } g^{-1}$$

The practical specific capacity of 477.87 mAh g^{-1} for Sb_2O_3@Sb@NC at the fifth cycle under 0.5 A g^{-1} was very closed to 479.45 mAh g^{-1} (**Fig. 3b**), indicating the accuracy of above equation. Consequently, the capacity contribution Sb_2O_3, Sb, and NC in the Sb_2O_3@Sb@NC composite could be approximately calculated to 345.57, 121.37 and 56.31 mAh g^{-1}, respectively.

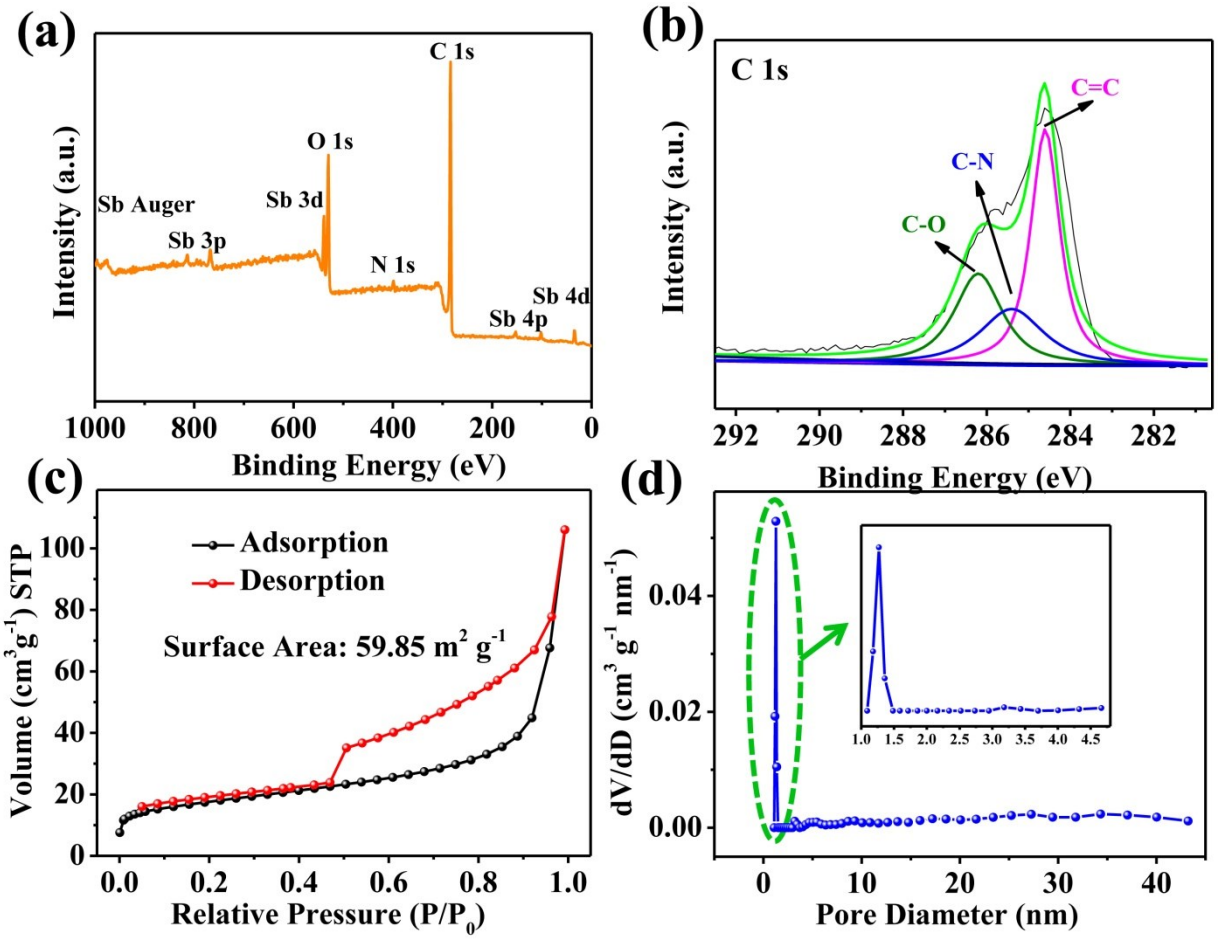

Fig. S5 (a) Survey XPS spectrum, (b) C 1s spectrum, (c) nitrogen isotherm plots and (d) pore volume distribution curves of the Sb_2O_3@Sb@NC composite.

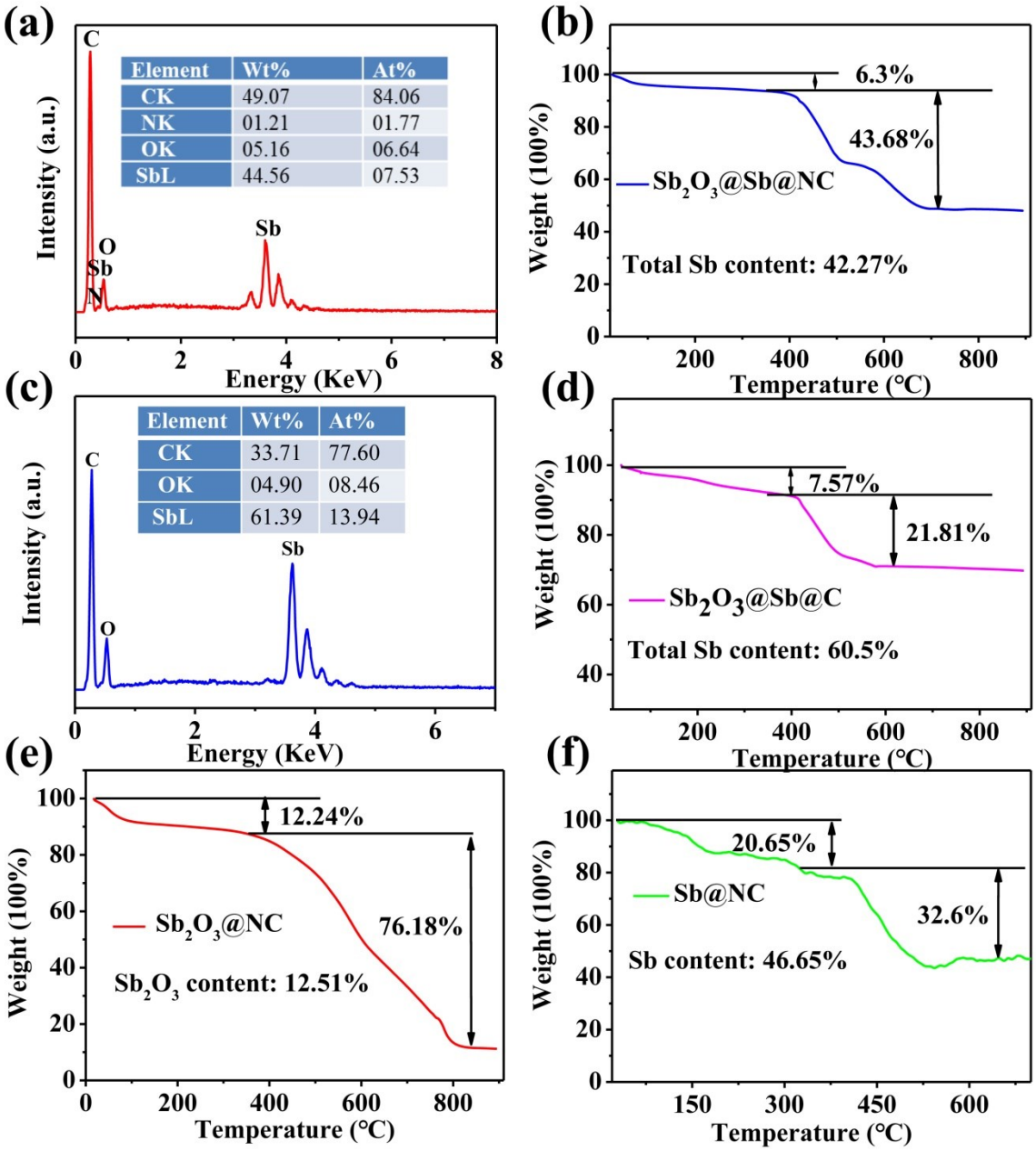

Fig. S6 EDS analysis of (a) Sb_2O_3@Sb@NC and (c) Sb_2O_3@Sb@C composite; TG analysis of (b) Sb_2O_3@Sb@NC, (d) Sb_2O_3@Sb@C, (e) Sb_2O_3@NC, and (f) Sb@NC composites tested in the air atmosphere.

For the Sb_2O_3@Sb@NC and Sb_2O_3@Sb@C composite, TG analysis showed that the total Sb content in two materials was 42.27% and 60.5%, respectively. The weight ratio of Sb_2O_3:Sb could be quantitatively analyzed from their XRD intensity ratio because the mass fraction of specific phase is directly proportional to its diffraction peak intensity in a mixed phase. Therefore, The weight ratio of Sb_2O_3:Sb in the Sb_2O_3@Sb@NC and Sb_2O_3@Sb@C composites could be calculated

to be 1.217 and 1.513 from their diffraction peak intensity ratio. Consequently, the mass fraction of metallic Sb, Sb_2O_3, and N-doped carbon in the Sb_2O_3@Sb@NC composite could be calculated as 20.96, 25.51, 53.53wt%. In the Sb_2O_3@Sb@C composite, the content of Sb, Sb_2O_3, and C could be calculated as 26.73, 40.44 and 32.83 %, respectively. TG analysis of the total Sb and C content in two materials was very close to that of EDS analysis results, indicating the above analysis of material composition is relatively accurate.

For the Sb_2O_3@NC and Sb@NC composite, we can calculate the final product of Sb_2O_4 after Sb and Sb_2O_3 oxidation in the air to analyze the mass fraction of materials. As a result, the Sb_2O_3 content in the Sb_2O_3@NC and the component of Sb in the Sb@NC composite could be calculated as 12.51% and 46.65%, respectively. The relatively lower Sb_2O_3 content in the Sb_2O_3@NC composite might be mainly attributed to the lower degree of carbonization at 450 ^oC.

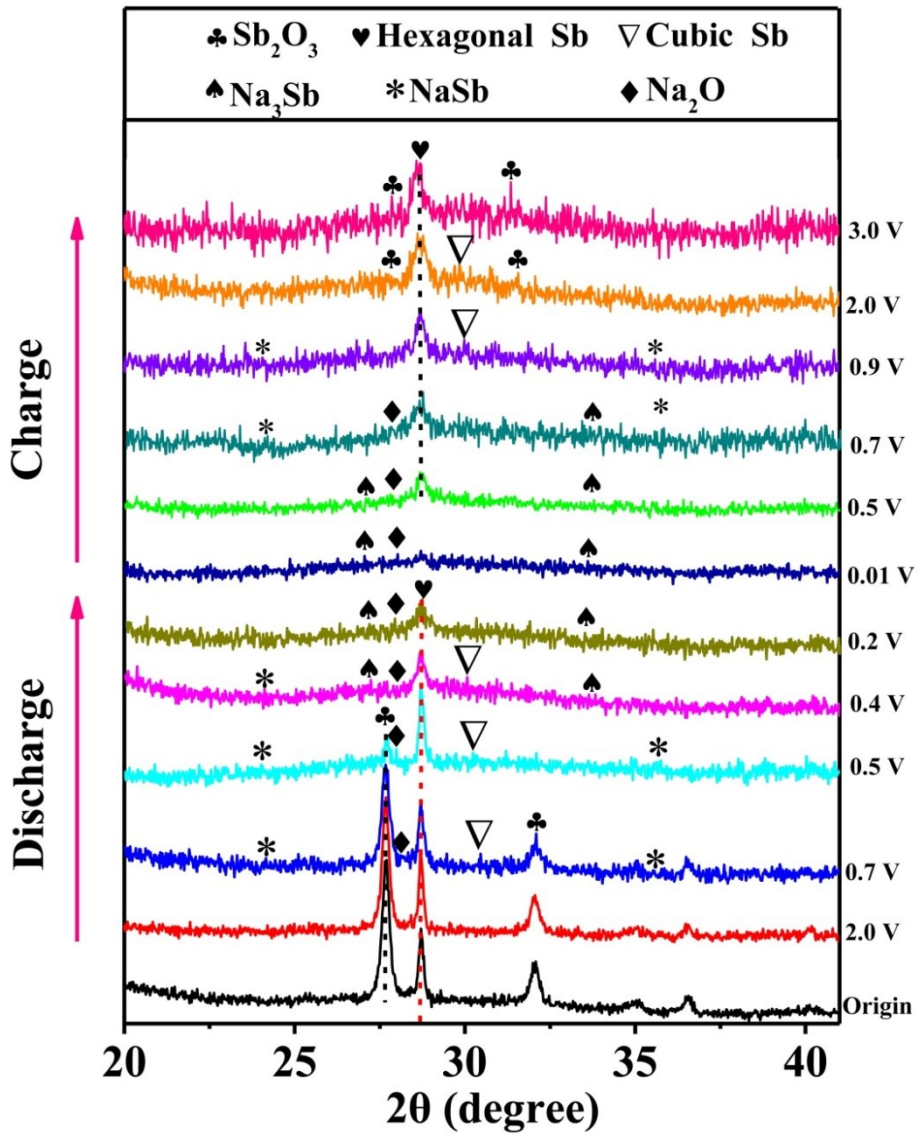

Fig. S7 *Ex situ* XRD patterns of the Sb_2O_3@Sb@NC electrode at different discharge-charge stages for sodium ion batteries.

Ex situ XRD techniques were adopted to explore the storage mechanism of sodium for Sb_2O_3@Sb@NC. As shown in **Fig. S7**, some typical peaks at specific voltages were conducted to detect XRD patterns measured from 20° to 41°. The origin material owned good crystallinity with sharp peaks and well indexed to the Sb_2O_3 (JCPDS No. 43-1071) and hexagonal Sb (JCPDS No. 35-0732). Upon the initial insertion of Na^+, the intensity of Sb_2O_3 gradually decreased. And simultaneously, the peaks around 27.95° corresponding to the Na_2O (JCPDS No. 03-1074), the peaks of NaSb located at 24.5° and 35.3° (JCPDS No. 74-0801) and cubic Sb (JCPDS No. 17-0125)

were explicitly detected, indicating the emergence of conversion reaction of Sb_2O_3 to form Na_2O and cubic Sb, and following alloy reaction of Sb. With the further discharge processing, the diffraction peaks of Sb_2O_3 gradually disappeared, while the weak peaks at 26.83° were ready to sprout resulting from the formation Na_3Sb (JCPDS No. 04-0724). When the voltage decreased to 0.01V, the phase of original Sb_2O_3 and Sb were not observed, the peaks of Na_3Sb and Na_2O could be still found.

At the charge process, the peak of Sb was gradually recovered due to the desodation at low potential. The peaks intensity of Na_3Sb phase and Na_2O piecemeally decreased and the peaks of NaSb were detected by degree. With the Na^+ extraction continuing, the peak of NaSb was weaken and the cubic Sb reappeared and existed until finally disappeared from its characteristic position. At the fully-charged state, the peaks of original Sb_2O_3 with (400) plane at 32.01° and hexagonal Sb were detected, suggesting that Sb_2O_3@Sb@NC owned the outstanding cyclic reversibility. The *ex situ* XRD results was consistent with the CV investigation.

From *ex situ* XRD results, the sodium storage mechanism for the Sb_2O_3@Sb@NC could be clearly demonstrated as follows:

Discharging reactions:

$$Sb_2O_3 + 6Na^+ + 6e^- \rightarrow 2Sb\ (cubic) + 3Na_2O \quad (1)$$

$$Sb\ (cubic\ and\ hexagonal) + Na^+ + e^- \rightarrow NaSb \quad (2)$$

$$NaSb + 2Na^+ + 2e^- \rightarrow Na_3Sb \quad (3)$$

Charging reactions:

$$Na_3Sb - 2Na^+ - 2e^- \rightarrow NaSb \quad (4)$$

$$NaSb - Na^+ - e^- \rightarrow Sb\ (cubic\ and\ hexagonal) \quad (5)$$

$$2Sb\ (cubic) + 3Na_2O - 6Na^+ - 6e^- \rightarrow Sb_2O_3 \quad (6)$$

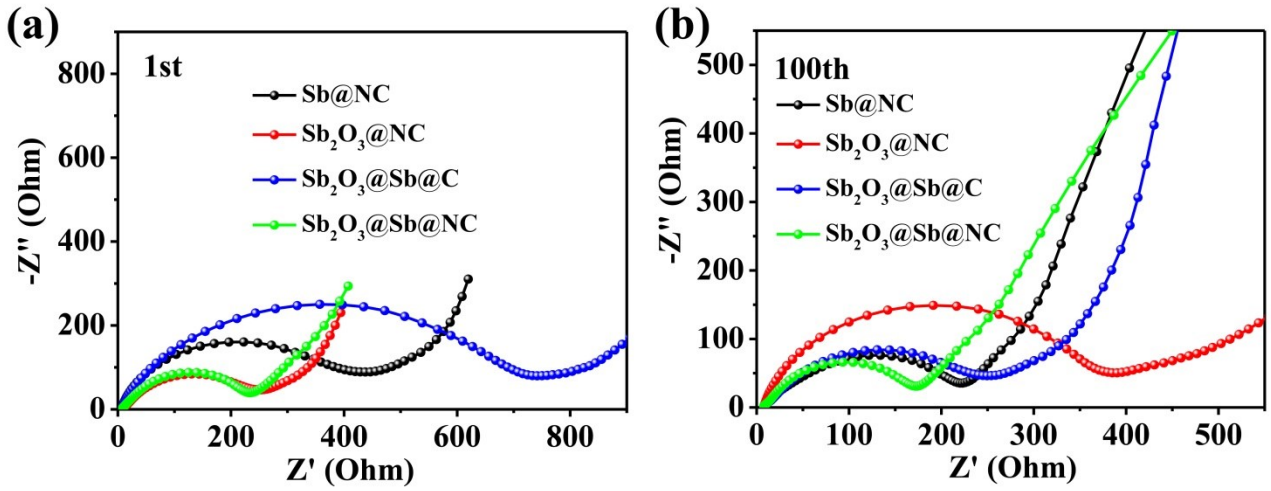

Fig. S8 EIS profiles (a) at 1st and (b) 100th cycle for Sb_2O_3@Sb@NC, Sb@NC, Sb_2O_3@NC, Sb_2O_3@Sb@C under a current density of 10 A g^{-1}.

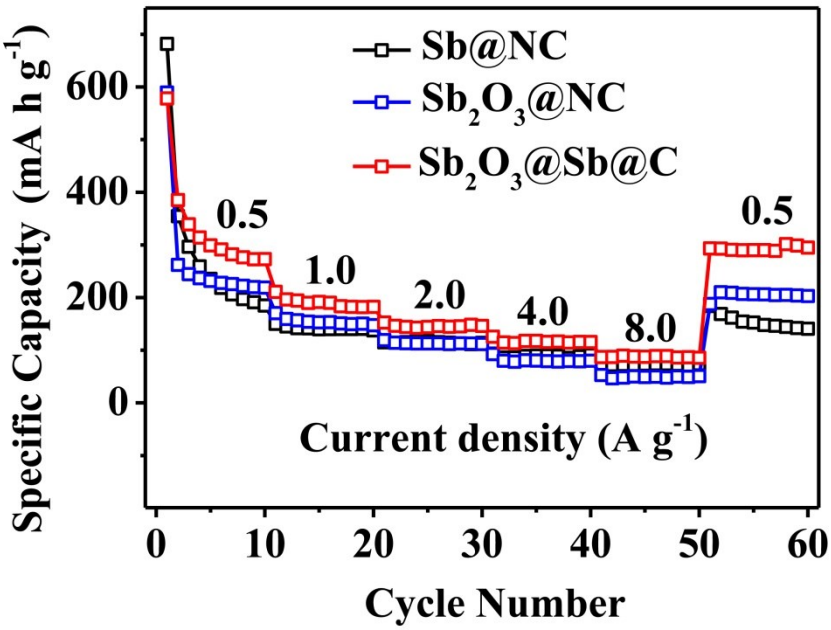

Fig. S9 The rate performance of sodium ion batteries for Sb@NC, Sb_2O_3@NC, Sb_2O_3@Sb@C, under different current densities.

As a comparison, Sb@NC, Sb_2O_3@NC, Sb_2O_3@Sb@C composites displayed reversible capacities of 259.1, 141.0, 118.4, 89.0, 73.4, 147.9 mAh g^{-1}; 262.1, 156.7, 112.8, 80.9, 50.1, 206.2 mAh g^{-1}; and 385.1, 190.1, 146.0, 117.7, 89.7, 298.8 mAh g^{-1} under 0.5, 1.0, 2.0, 4.0, 8.0, 0.5 A g^{-1}, respectively. Remarkably, Sb_2O_3@Sb@NC showed a high reversible capacity of 175.1 mAh g^{-1}

even the current density increased to ultrahigh rate of 20 A g^{-1}, showing impressive enhanced kinetics and ultrahigh rate capability than the above control samples.

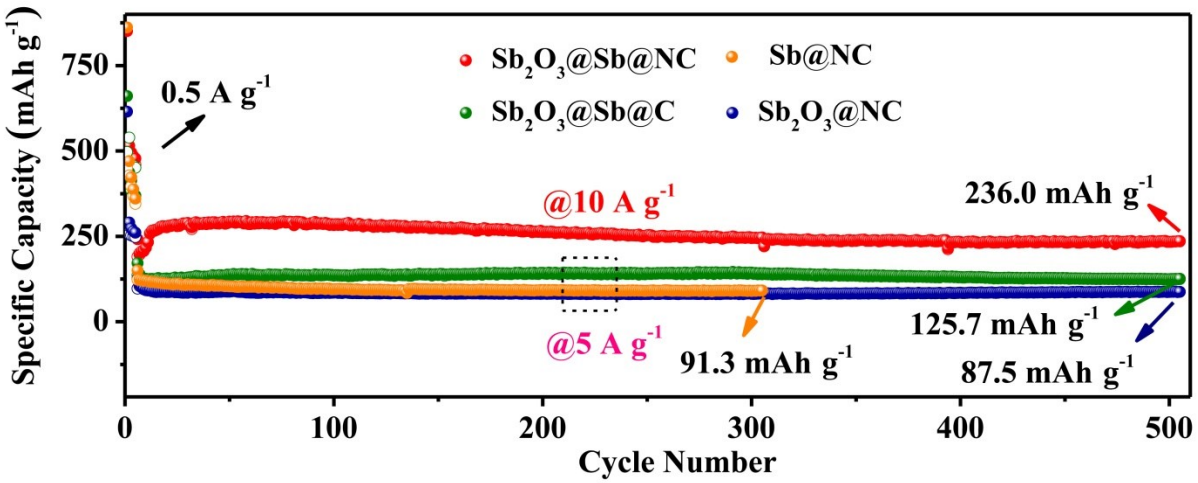

Fig. S10 The cycling performance of sodium ion batteries for Sb_2O_3@NC, Sb_2O_3@Sb@C, Sb_2O_3@Sb@NC and Sb@NC composites under different current densities.

With a comparison of cycling performance, Sb_2O_3@ NC, Sb_2O_3@Sb@C and Sb@NC composites delivered lower reversible capacities of only 87.5 mAh g^{-1}, 125.7 mAh g^{-1} at 505th cycle and 91.3 mAh g^{-1} at 305th cycles under 5 A g^{-1}, respectively. Impressively, Sb_2O_3@Sb@NC electrode could deliver a higher capacity of 236.0 mAh g^{-1} at 505th cycle under ultra-high rate of 10 A g^{-1}. These results indicated that the introduction of Sb_2O_3@Sb heterojunction and N-doping was beneficial for sodium storage performance under ultra-high current density, and also consistent with the date analyzed by DFT theory.

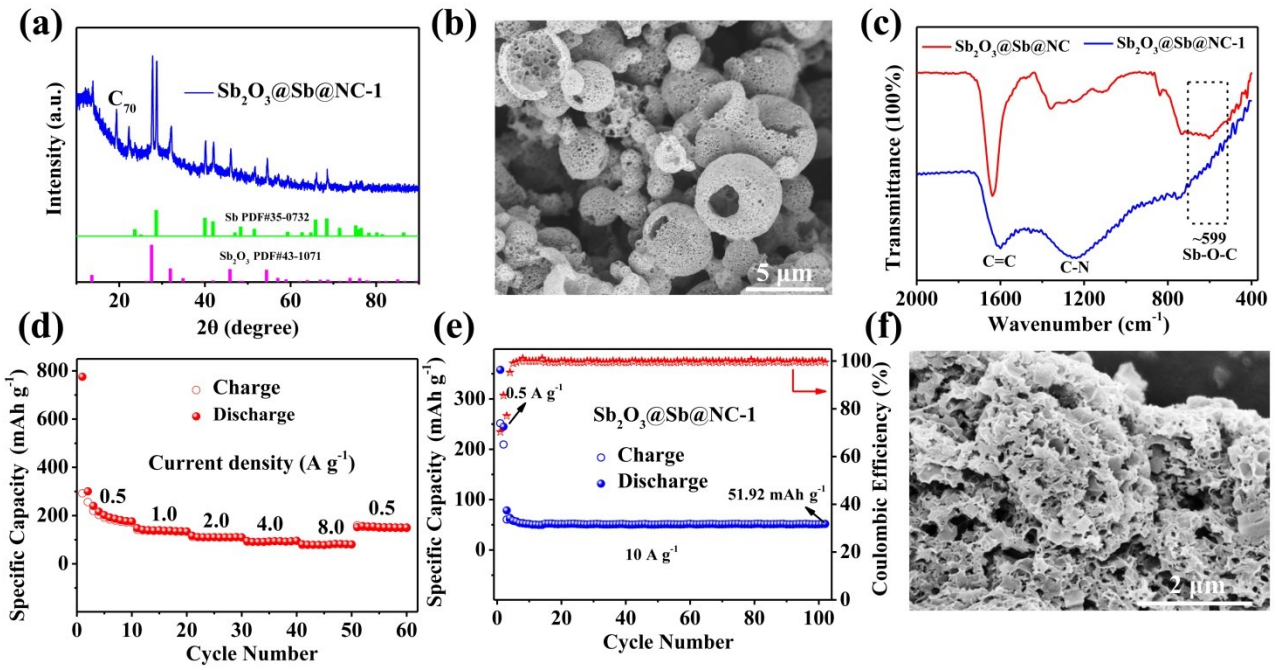

Fig. S11 (a) XRD, (b) SEM, (c) FT-IR, (d) rate performance, (e) cycling performance of Sb_2O_3@Sb@NC-1, and (f) SEM of Sb_2O_3@Sb@NC-1 after 100 cycles at the current density of 10 A g^{-1}.

To investigate the influence of Sb-O-C bond on structure integrity and electrochemical performance, Sb_2O_3@Sb@NC-1was synthesized by adding the hard template of NaCl instead of KCl. As we can see, Sb_2O_3@Sb@NC-1 reserved analogous structure and characteristic XRD peaks of Sb_2O_3@Sb@NC. However, the FT-IR spectrum of Sb_2O_3@Sb@NC-1 could not be observed the stretching vibration peak of Sb-O-C bond around 599 cm^{-1}, illustrating that KCl is not only used as a template but also as an activator of forming Sb-O-C bond. Obviously, Sb_2O_3@Sb@NC-1 displayed the poor rate performance lower output capacity compared with Sb_2O_3@Sb@NC (**Fig.3**), *e.g.,* 78.7 mAh g^{-1} at 8 A g^{-1} and 51.92 after 100 cycles at 10 A g^{-1}. What's more, the completely broken materials of Sb_2O_3@Sb@NC-1 after only 100 cycles at 10 A g^{-1} indicated that it is difficult to maintain the structure integrity without the chemical coupling Sb-O-C bond.

On the basis of above discussion, there's no denying that the strong interfacial Sb-O-C bond

provided positive effect for enhanced cycle stability, rate performance and robust material structure integrity.

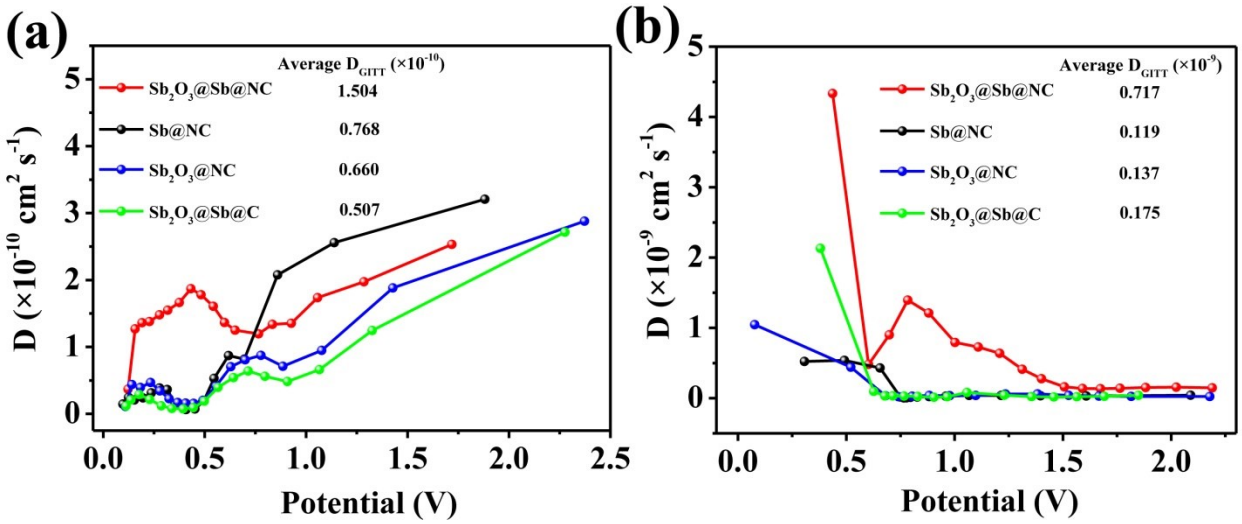

Fig. S12 (a) Discharge-state and (b) charge-state diffusion coefficient values of Sb@NC, Sb_2O_3@NC, Sb_2O_3@Sb@C compared with Sb_2O_3@Sb@NC under 500 mA g^{-1} tested by GITT.

Galvanostatic intermittent titration technique (GITT) has been adopted to deeply check electrochemical kinetics of the Sb_2O_3@Sb@NC electrode in sodium and potassium ion batteries. During GITT process, the testing cells were discharged or charged at the current density of 500 mA g^{-1} for 2 minutes and then taken a relaxation of 10 minutes. The ion diffusion coefficient can be calculated by the simplified formula:

$$D_{GITT} = \frac{4L^2}{\pi\tau}\left(\frac{\Delta E_s}{\Delta E_\tau}\right)^2 \qquad \text{(Equation 1)}$$

where τ is the current pulse time; L is the thickness of electrode materials; ΔE_s is the steady-state voltage change after current pulse, and ΔE_τ represents the voltage change during the current pulse excluding the IR-drop.[1, 2]

In the discharge state, Sb_2O_3@Sb@NC, Sb@NC, Sb_2O_3@NC,and Sb_2O_3@Sb@C owned average diffusion coefficient values of 1.504×10^{-10}, 0.768×10^{-10}, 0.660×10^{-10} and 0.507×10^{-10}

$cm^2\ s^{-1}$, respectively. Furthermore, Sb_2O_3@Sb@NC also displayed overwhelmed preponderance on average diffusion coefficient values in the charge state than that of them. The above results revealed that the synergistic effect of introducing heterostructures and N-doping could enhance the Na^+ diffusion coefficient and further improve the electrochemical performance.

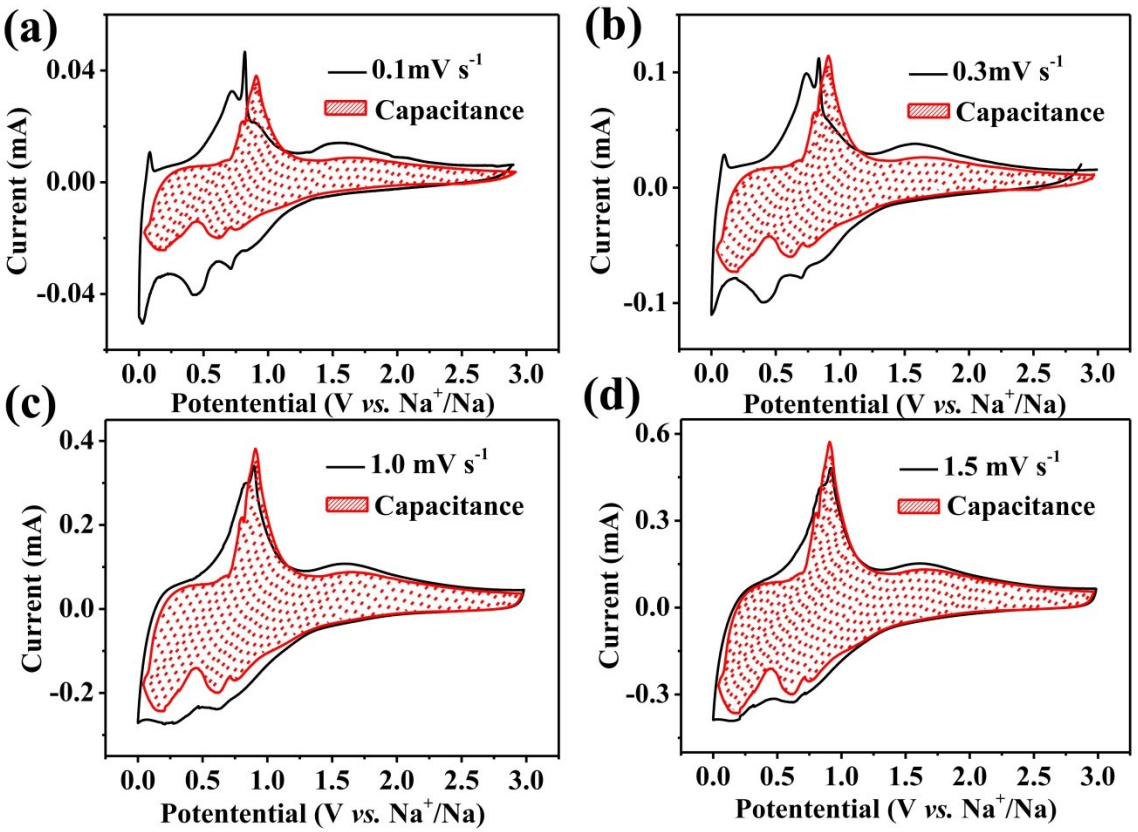

Fig. S13 The accurately theoretical calculations on capacitive-effect contribution (red shadow area) to total sodium-storage capacity at a sweep rate of (a) 0.1, (b) 0.3, (c) 1.0 and (d)1.5 mV s^{-1}.

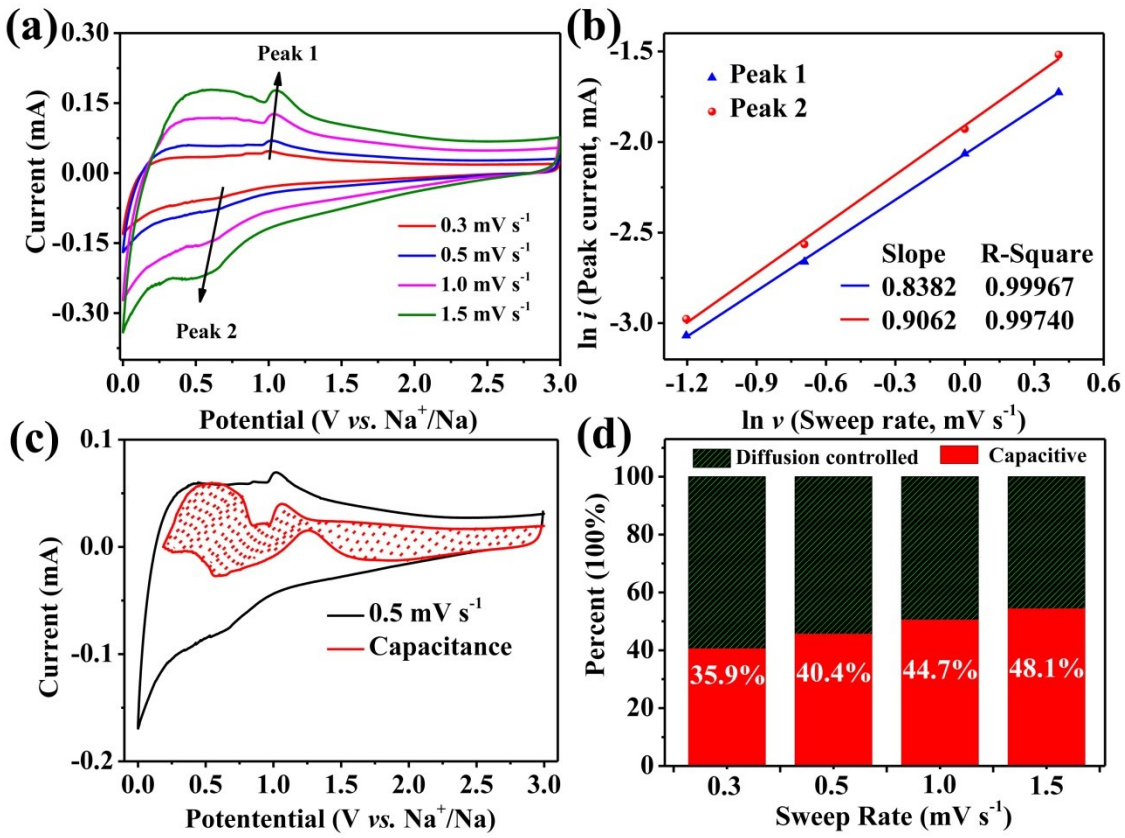

Fig. S14 The accurately theoretical calculations on capacitive-effect contribution for Sb@NC composites. (a) CV curves with different sweep rates after 50 discharge/charge cycles at high current density of 10 A g^{-1} for SIBs, (b) the line relationship of ln(*i*, peak density) *vs.* ln(*v*, sweep rate) at peak 1-2, (c) the capacitive contribution to total sodium-storage capacity (shadow area) at a sweep rate of 0.5 mV s^{-1}, (d) the percentage of capacitive contribution at different rates.

From above theoretical calculations of capacitive effect, the pseudocapacitance behavior during cycling in Sb@NC composites was partially contributed to total capacity. However, when the Sb_2O_3 was introduced into Sb@NC to form Sb_2O_3@Sb@NC, the capacitive contribution of Sb_2O_3@Sb@NC was very higher than that Sb@NC, *e.g.,* 73.8% *vs.* 40.4% at the scan rate of 0.5 mV s^{-1}, implying that the solid-solid interface of Sb_2O_3@Sb could provide extra interfacial pseudocapacitance.

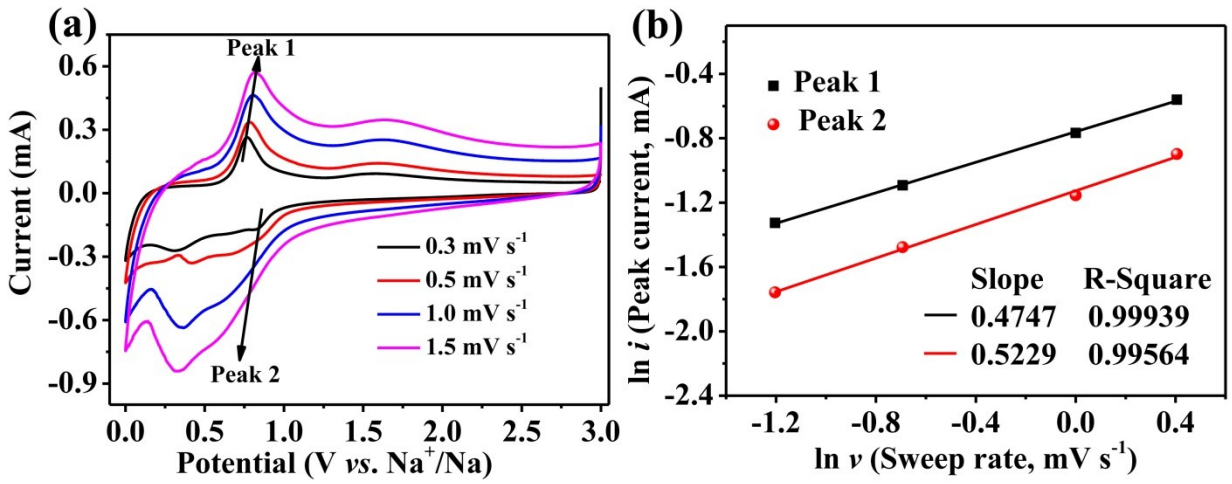

Fig. S15 The accurately theoretical calculations on capacitive-effect contribution for Sb_2O_3@NC composites. (a) CV curves with different sweep rates after 50 discharge/charge cycles at high current density of 10 A g^{-1} for SIBs, (b) the line relationship of ln(*i*, peak density) *vs.* ln(*v*, sweep rate) at peak 1-2.

The capacitive-effect contribution could be assessed by the CV curves of Sb_2O_3@NC electrode at various sweep rates (**Fig. S15a**). The relation between the current (*i*) and sweep rate (*v*) could be described by the power equation: $i=av^b$, where *a* value and *b* value are adjustable quantities. The *b* value can be obtained from the slop of the fitted plot in the **Fig. S15b** (herein, b=0.5, extreme diffusion-controlled behavior; b=1, classic pseudocapacitance-controlled process).

The average line slope of peak 1 and peak 2 from the relationship of ln *i* *vs.* ln *v* could be calculated to be 0.4988, implicating the cycling process of Sb_2O_3@NC electrode is a type of extreme diffusion-controlled behavior. However, when the Sb was introduced into Sb_2O_3@NC to form Sb_2O_3@Sb@NC, the essential ascension of capacitive contribution for Sb_2O_3@Sb@NC was obvious, indicating that the solid-solid interface of Sb_2O_3@Sb could really introduce extra interfacial pseudocapacitance.

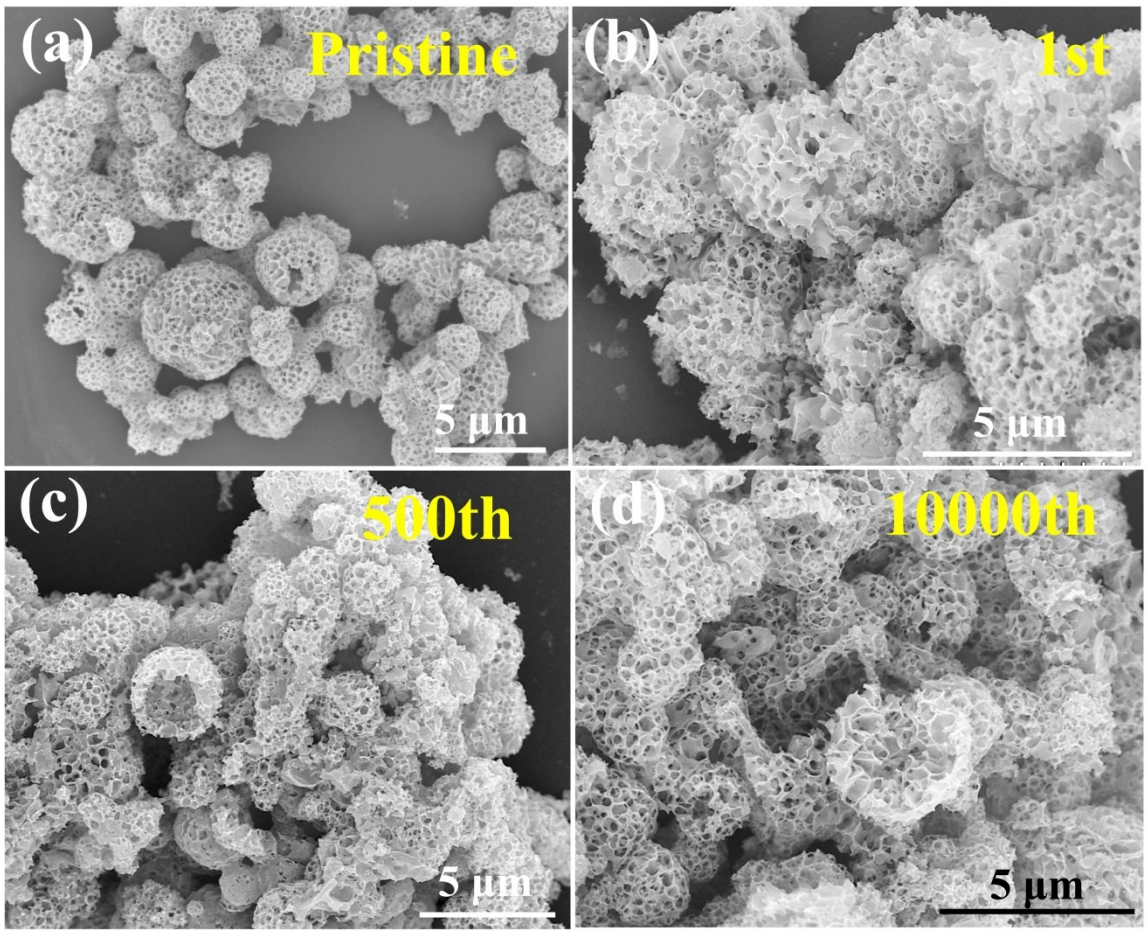

Fig. S16 SEM images of Sb_2O_3@Sb@NC electrode at (a) pristine, (b) 1st, (c) 500th, and (d) 10000th cycle under a high rate of 10 A g^{-1}.

As shown in **Fig. S16**, Sb_2O_3@Sb@NC electrode owned enviable structural stability with well-maintained original morphology after various cycles even undergoing 10000 cycles at high rate of 10 A g^{-1}. The outstanding structure preserving might be ascribed to the tightly packaged active materials by porous carbon networks and the cohering strong chemical bond of Sb-O-C, ensuring the long-term cycling stability and ultrahigh rate performance.

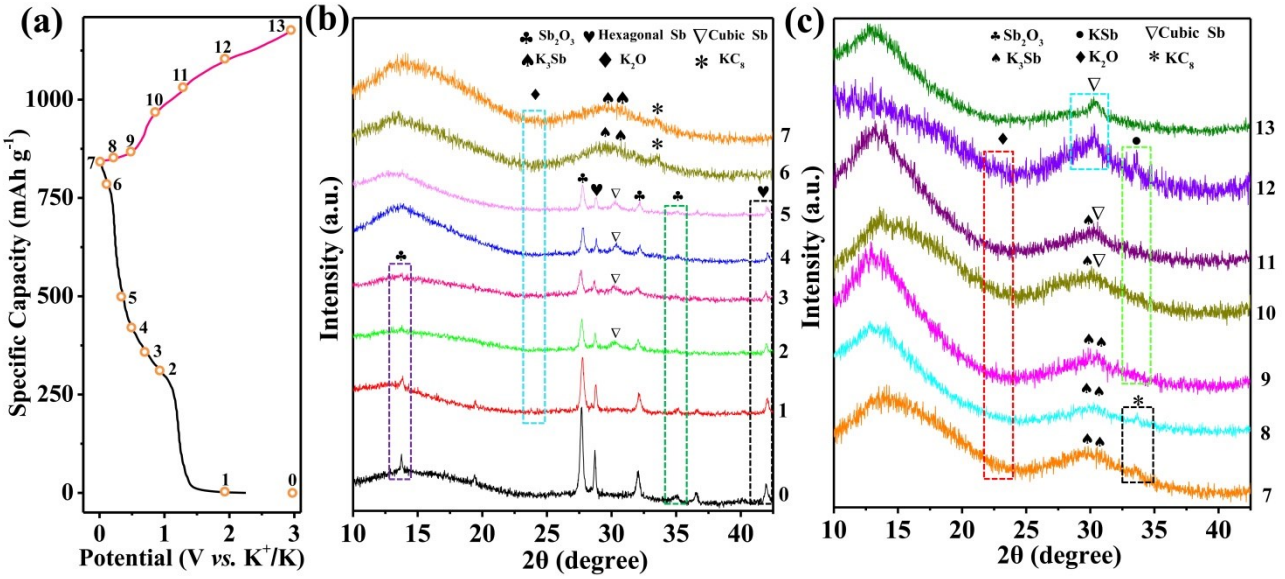

Fig. S17. (a) The first discharge/charge curves of Sb_2O_3@Sb@NC electrode at 0.1 A g^{-1} for potassium ion battery, (b-c) *ex situ* XRD patterns of the Sb_2O_3@Sb@NC electrode at different discharge-charge stages.

Based on detail discuss of the superior electrochemical sodium storage performance, the investigation into potassium storage properties of the Sb_2O_3@Sb@NC composites also attracted our interest. Up to now, the potassium storage mechanism of antimony-oxide-based heterojunction was not clear. *Ex-situ* XRD techniques were adopted to explore the electrochemical mechanism of the Sb_2O_3@Sb@NC before deep discussions. As shown in **Fig. S17a-c**, some typical points at different voltages were adopted to detect XRD patterns measured from 10° to 42.5°. Before the discharge test, the origin material owned good crystallinity with sharp peaks and well indexed to the Sb_2O_3 (JCPDS No. 43-1071) and hexagonal Sb (JCPDS No. 35-0732). Upon the initial insertion of K^+, the intensity of Sb_2O_3 and hexagonal Sb gradually decreased, and simultaneously, the peaks at around 23.9° and 30.38° respectively corresponding to the K_2O (JCPDS No. 23-0493) and cubic Sb (JCPDS No. 17-0125) were explicitly detected, indicating the emergence of conversion reaction of Sb_2O_3 to K_2O and cubic Sb (**Fig. S17b**). With the further discharge processing, the diffraction peaks of Sb_2O_3 and Sb gradually disappeared, while the weak peaks at 29.6° and 30.3° were ready to

sprout due to the gradual formation K_3Sb (JCPDS No. 04-0643). As the K^+ insertion going on, the phase of KC_8 was detected with a broad peak at 33.6°, illustrating that carbon matrix was also involved in the electrochemical reaction. At the charge process (**Fig. 17c**), the peaks of KC_8 quickly vanished due to the depotassiation at low potential. Accompanying with it, the peak intensity of K_3Sb phase gradually decreased along with the appearance of KSb around 34.1° (JCPDS No.41-1289). With the K^+ extraction continuing, the peak of K_3Sb was faded out and finally failed to find itself at aforementioned position in XRD pattern, with the reoccurrence of cubic Sb originated from following deep depotassiation. At the fully-charged state, the above peaks of KSb, K_3Sb and K_2O eventually vanished, and no sharp peaks of original Sb_2O_3 were detected, suggesting that the primary Sb_2O_3 phase might have been converted into amorphous species. Instead, the relative higher peak of cubic Sb was clearly observed. Moreover, the XPS spectra of Sb 3d for the Sb_2O_3@Sb@NC in the full charge state confirmed the existence of Sb_2O_3 phase (**Fig. S18**).

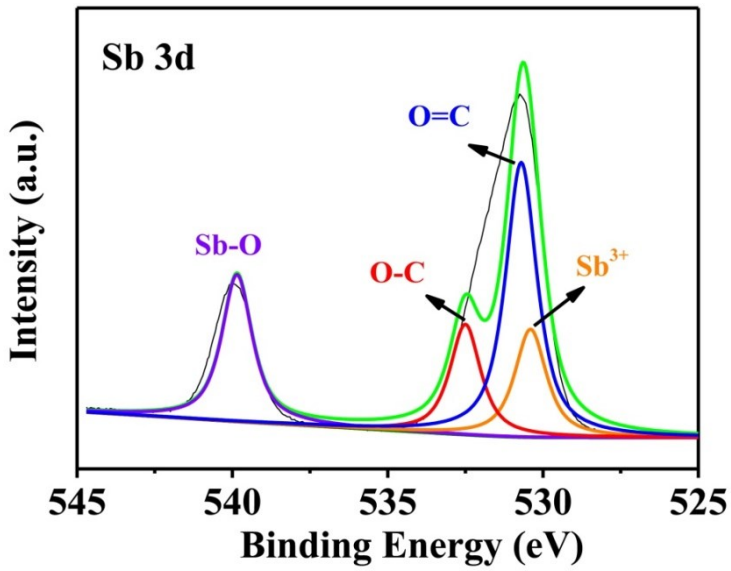

Fig. S18 XPS spectra of Sb 3d for the Sb_2O_3@Sb@NC in the full charge state at 100 mA g^{-1}.

Fig. S19a exhibited the initial three CV curves for potassiation/depotassiation of Sb_2O_3@Sb@NC electrode in the voltage range of 0.01-3 V at the scan rate of 0.1 mV s^{-1}. At the

first cycle, three reduction peaks at 1.13 V, 0.86 V, and 0.21 V could be observed. The first one was ascribed to the formation of SEI film and the insertion of K^+ into Sb_2O_3 to form cubic Sb and K_2O.[3] And other two peaks were assigned to the multistep formation of KSb and K_3Sb.[4] In following anodic sweeping, three anodic peaks at 0.66 V, 1.10 V and 1.72 V corresponded to the extraction of potassium ions from K_3Sb, KSb and the subsequent formation of Sb_2O_3 by the electrochemical reaction between cubic Sb and K_2O,[3, 5, 6] respectively. In the next cathodic scans, there aroused three fresh reduction peaks at 1.16 V, 0.64 V and 0.13 V, which always existed in subsequent cathodic scanning. Such three peaks could be attributed to the multistep insertion of potassium ions to form cubic Sb and K_2O, KSb and K_3Sb, respectively.[7, 8] A couple of redox peaks at 0.01V and ~0.15 V were associated with the K^+ insertion/extraction for the carbon matrix.

Combining CV with *ex situ* XRD results, the potassium storage mechanism for the Sb_2O_3@Sb@NC is clearly demonstrated as follows, which contains multistep conversion reactions and alloying processes:

Discharging reactions:

$$Sb_2O_3 + 6K^+ + 6e^- \rightarrow 2Sb\ (cubic) + 3K_2O \quad (1)$$

$$Sb\ (cubic\ and\ hexagonal) + K^+ + e^- \rightarrow KSb \quad (2)$$

$$KSb + 2K^+ + 2e^- \rightarrow K_3Sb \quad (3)$$

$$8C + K^+ + e^- \rightarrow KC_8 \quad (4)$$

Charging reactions:

$$KC_8 - K^+ - e^- \rightarrow 8C \quad (5)$$

$$K_3Sb - 2K^+ - 2e^- \rightarrow KSb \quad (6)$$

$$KSb - K^+ - e^- \rightarrow Sb\ (cubic) \quad (7)$$

$$2Sb\ (cubic) + 3K_2O - 6K^+ - 6e^- \rightarrow Sb_2O_3\ (amorphous) \quad (8)$$

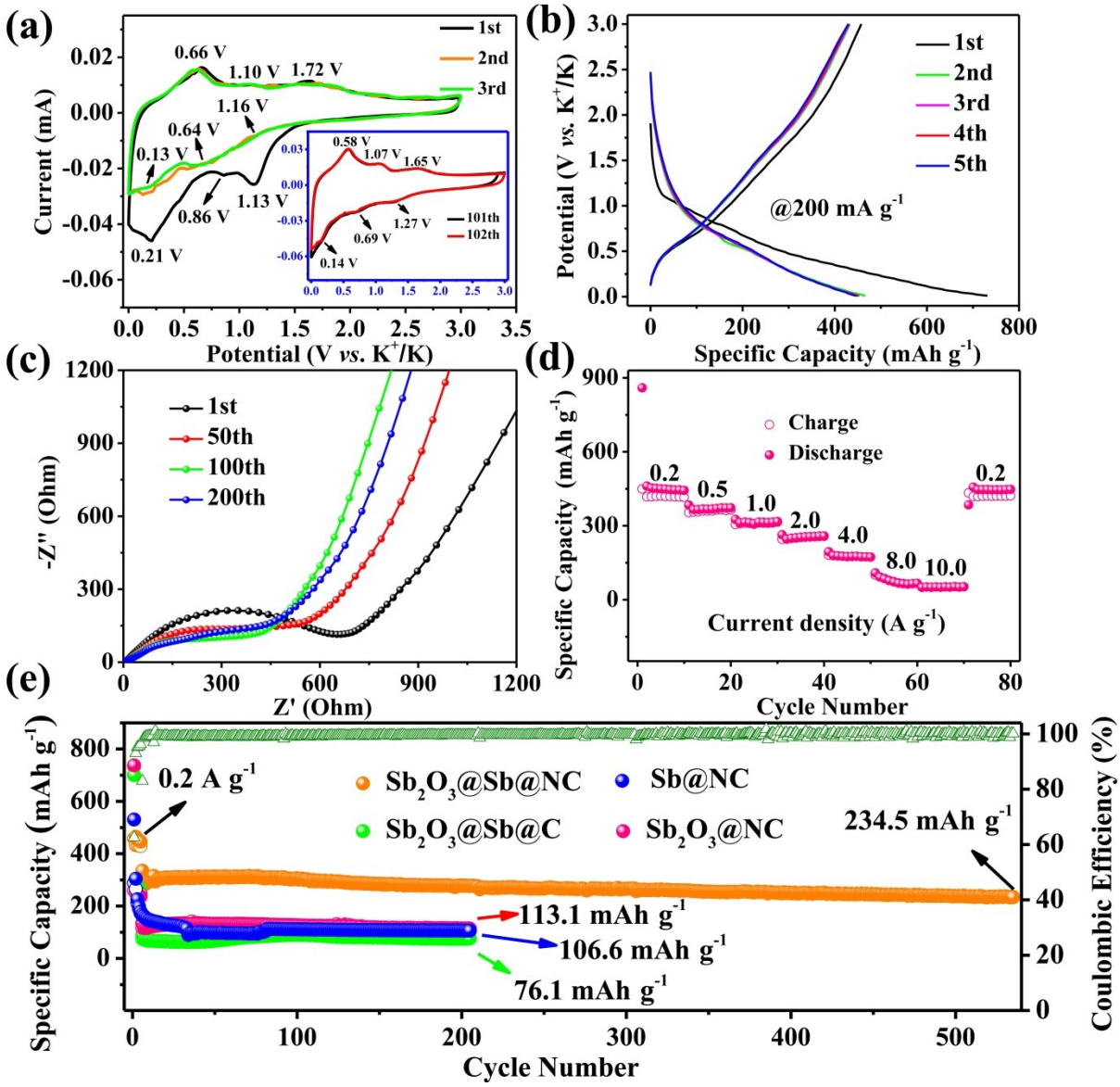

Fig. S19 Electrochemical performance of Sb_2O_3@Sb@NC electrode for PIBs. (a) CV curves at a scan rate of 0.1 mv s^{-1} in the voltage range of 0.0-3.0 V, the inserted graph is the CV curves after 101 and 102 cycles at 200 mA g^{-1}; (b) galvanostatic charge/discharge curves at 200 mA g^{-1}; (c) EIS profiles after various cycles at a current density of 2 A g^{-1}; (d) rate capability at different densities from 0.2 to 10.0 A g^{-1}; (e) cycling performance at high current density of 2 A g^{-1}.

Importantly, after cycling more than 100 cycles, the cathodic peaks of CV curves shifted to 1.27 V, 0.69 V, and 0.14 V, while the corresponding anodic peaks shifted to 1.65 V, 1.07 V, and 0.58 V. The potential difference between redox couples became universally smaller after long-term

cycling, *e.g.,* 0.44 V at 100th cycle *vs.* 0.53 V at second cycle under low potential reaction, clearly indicating the attenuation of polarization effect with cycling number increasing. Such an undeniable fact demonstrated the appearance of enhanced kinetics and improved reversible capability upon potassiation/depotassiation. Meanwhile, the completely overlapped CV curves and the first five galvanostatic charge/discharge profiles at the current of 200 mA g^{-1} (**Fig. S19b**) ulteriorly confirmed the stable cycling stability of the Sb_2O_3@Sb@NC composites.

The EIS profiles of the electrode under the current of 2 A g^{-1} at different cycles were also investigated to explore the electrochemical kinetic and cycling capability (**Fig. S19c**). Similar to sodium ion battery, the Sb_2O_3@Sb@NC electrode also presented the gradually decreased charge-transfer resistance and increased line slope from 1st to 100th cycle, and simultaneously there is no distinct difference between 100th cycle and 200th cycle profile. All of which indicated the real exist of enhanced kinetic and improved reversible capability during cycling, which was consistent with the analysis of CV curves. Those features could lead to the ultra-fast K^+ insertion/extraction and superior cycling stability under high rate shock.

The rate capability of Sb_2O_3@Sb@NC electrode at various current densities was shown in **Fig. S19d**, which displayed excellent rate performance with high discharge capacities of 450.1, 383.9, 325.8, 263.5 194.8, and 109.0 mAh g^{-1}, at current densities of 0.2, 0.5, 1.0, 2.0, 4.0, 8.0 A g^{-1}, respectively. Remarkably, the Sb_2O_3@Sb@NC electrode could maintain 53.0 mAh g^{-1} even at the ultrahigh rate of 10.0 A g^{-1}. When the current density recovered to 0.2 A g^{-1}, the capacity could resumed to 456.8 mAh g^{-1}, revealing admirable electrochemical stability of the Sb_2O_3@Sb@NC electrode under successively high rate impact.

In order to further detect the durability of the Sb_2O_3@Sb@NC electrode under high current density, a long-term galvanostatic cycling test was performed at the current density of 2 A g^{-1}. As

presented in the **Fig. S19e**, the electrode afforded a high capacity of 445.8 mAh g-1 at a current density of 0.2 A g^{-1} after first 5 cycles. As to the following long-term cycling at the current density 2 A g^{-1}, Sb_2O_3@Sb@NC electrode possessed a great capability and rendered an impressive cycling stability with highly reversible capacity of 234.5 mAh g^{-1} after 530 cycles accompanied with high capacity retention of 82.1%. While the control samples, *i.e.*, Sb_2O_3@Sb@C, Sb_2O_3@NC and Sb@NC composites, only delivered lower capacities of 76.1 mAh g^{-1}, 113.1 mAh g^{-1} and 106.6 mAh g^{-1} at 2 A g^{-1} after 200 cycles, respectively. The robust cycling stability of Sb_2O_3@Sb@NC electrode was mainly attributed to the elaborately designed nature with the synergistic effect of Sb_2O_3@Sb heterojunction and N-doping and the strong chemical bond of Sb-O-C. The difference of electrochemical properties for sodium and potassium ion batteries was mainly attributed to the ionic radius and their difference of physicochemical property such as conductivity.

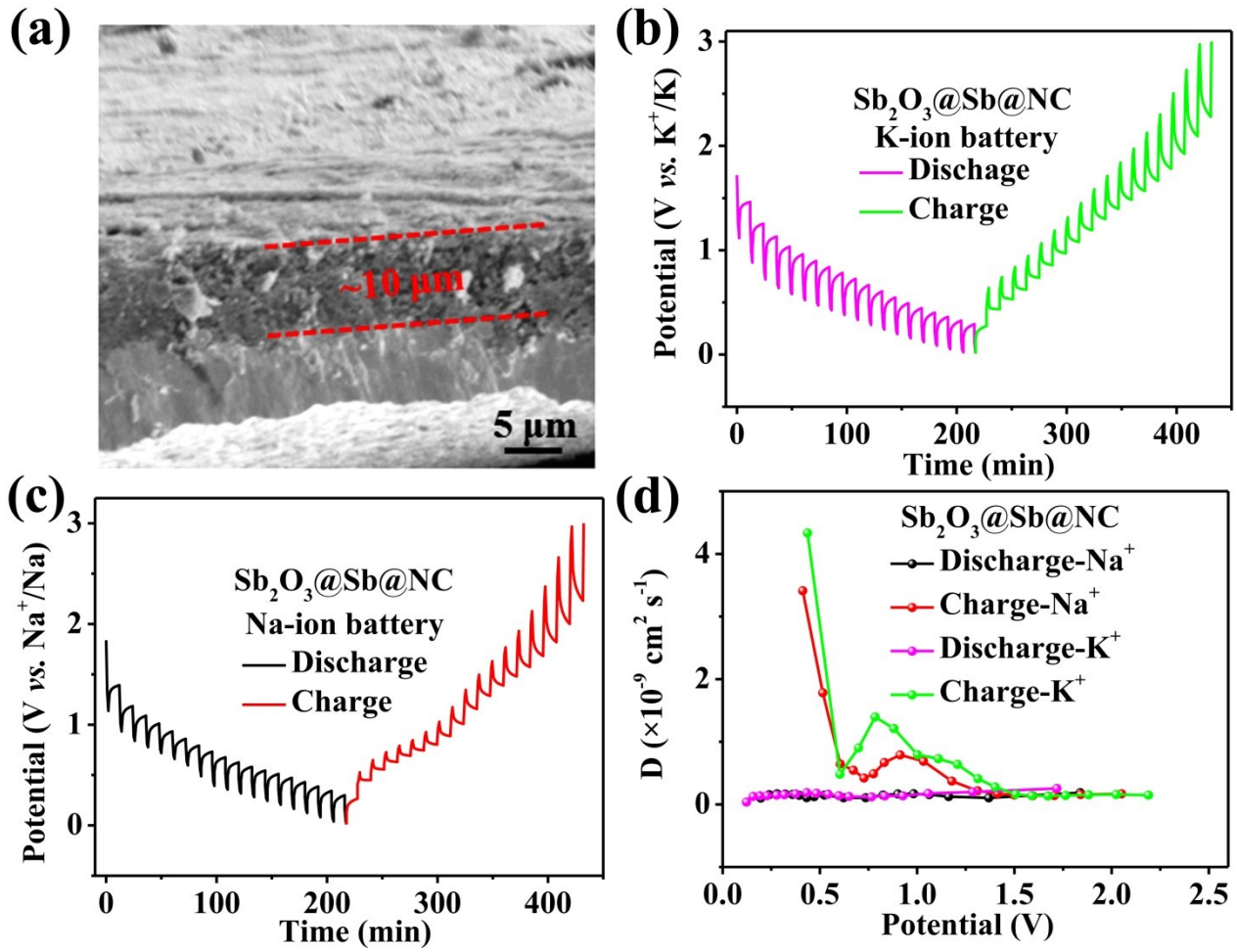

Fig. S20 (a) The thickness of Sb_2O_3@Sb@NC composite on the copper foil. GITT curves of Sb_2O_3@Sb@NC electrode for (a) PIBs, (b) SIBs, and (c) diffusion coefficient values of Na^+ and K^+ calculated from GITT tests.

Normally, the dynamic parameters for K^+ and Na^+ are supposed to very significantly different in the identical electrode material because of their discrepancy of ion radius and molar mass.[10] We have tested the GITT curves of Sb_2O_3@Sb@NC composite for potassium and sodium ion battery by Equation 1 (**Fig. S20a-c**). Surprisingly, we could observe that the average diffusion coefficient for K^+ and Na^+ of the Sb_2O_3@Sb@NC electrode is almost close in the same state of charge (SOC), regardless of discharging or charging (**Fig. S20d**), *e.g.,* 0.155×10^{-9} for SIBs and 0.174×10^{-9} cm^2 s^{-1} for KIBs at the same discharge state of 1.06 V. The inspiring result indicated that the unique structure advantage of Sb_2O_3@Sb@NC composite make itself own enough rapid

electrochemical kinetics to get rid of the restriction of ion radius difference when ions shuttled through electroactive materials at a current density of 500 mA g^{-1}.

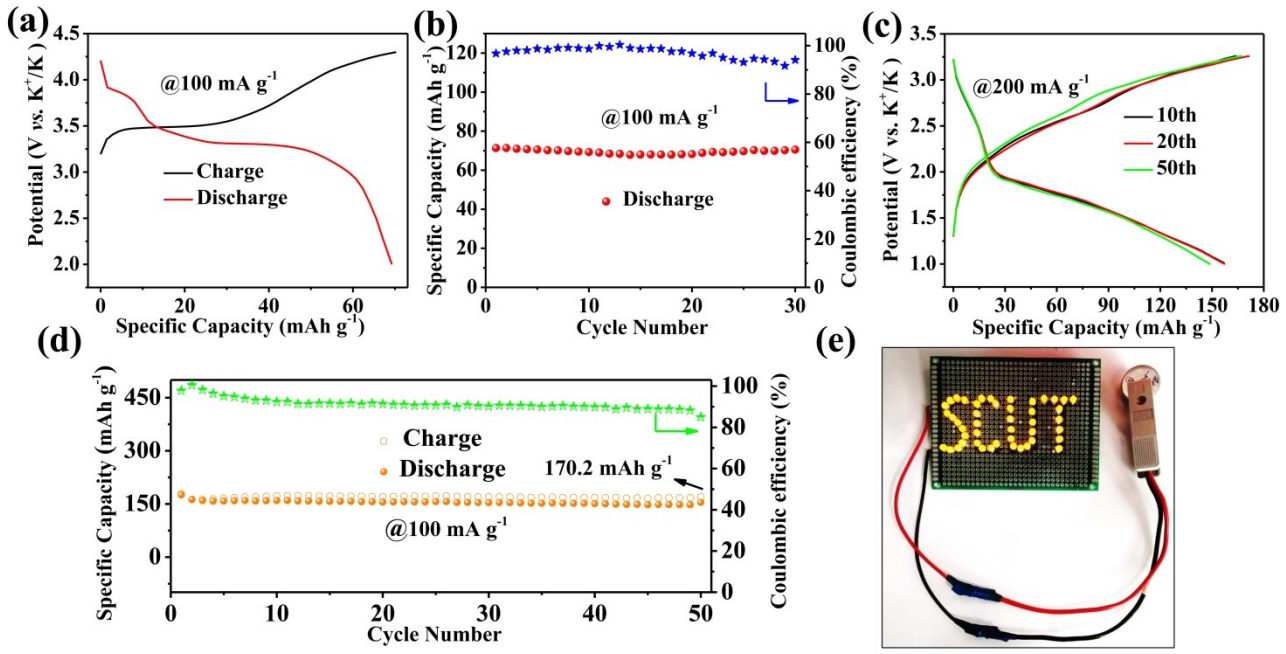

Fig. S21 (a) The galvanostatic charge/discharge profiles and (b) cycling performance at a current density of 100 mA g^{-1} of prussian white analogues cathode. (c) The galvanostatic charge/discharge profiles, (d) cycling performance at 100 mA g^{-1} and the photograph of lighting a bulb for the K^+ full cell.

In the full cell of PIB, prussian white analogues were adopted as cathodes, which owned a pair of plateau around 3.52/3.3 V (**Fig. S21a**) at current density of 20 mA g^{-1} and possessed stable output capacity of 70.5 mAh g^{-1} at 100 mA g^{-1} after 30 cycles (**Fig. S21b**). As the assembling full cell, the almost overlapped galvanostatic charge/discharge profiles demonstrated excellent stability with displaying a high capacity of 170.2 mAh g^{-1} at 100 mA g^{-1} after 50 cycles (**Fig. S21c-d**). And this full cell could lighten the light strip of "SCUT" constituted by yellow 47 LED bulbs, showing favorable prospect of practical application (**Fig. S21e**).

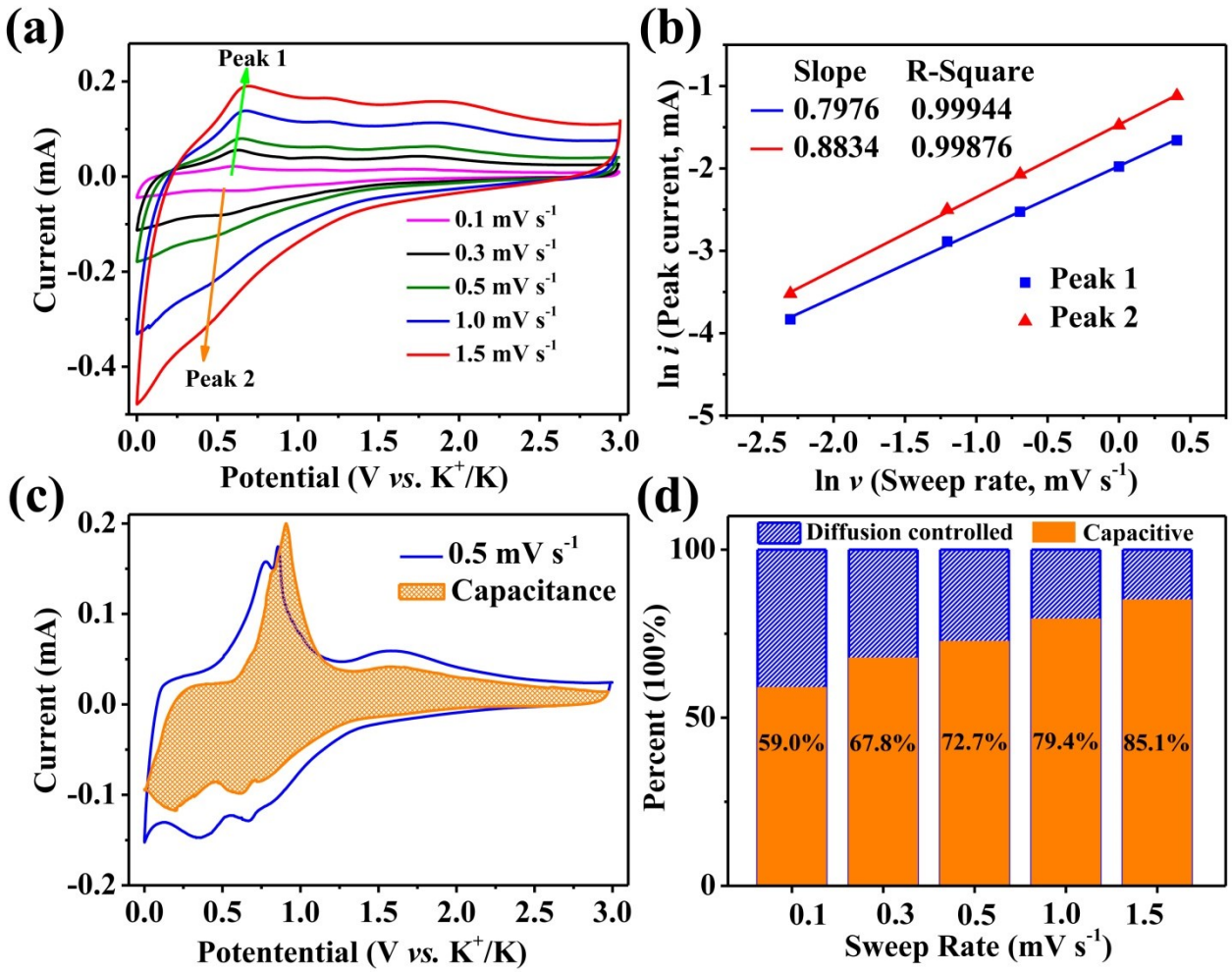

Fig. S22 (a) CV curves with different sweep rates after 50 discharge/charge cycles at high current density of 10 A g^{-1} for PIBs, (b) the line relationship of ln(*i*, peak density) *vs.* ln(*v*, sweep rate) at peak 1-2, (c) the capacitive contribution to total potassium-storage capacity (shadow area) at a sweep rate of 0.5 mV s^{-1}, (d) the percentage of capacitive contribution at different rates.

Table S1 Performance comparison of Sb-based materials between this work and literatures

Material	Synthetic method	Long cycle performance (mAh g^{-1} /A g^{-1} /cycle number)	Rate charge capacity (mAh g^{-1})/ Current density (A g^{-1})	Battery type	Ref.
Sb_2O_3@Sb@NC	**spray drying & hard template**	**245.2/10/10000** **234.5/2/530**	**175.1/20** **192.5/16** **109/8** **53/10**	**Sodium** **Potassium**	**This work**
Sb@C@TiO_2 triple-shell nanoboxes	template-engaged galvanic replacement approach	193/1/4000	212/10	Sodium	11
Sb/rGO-C	spray pyrolysis	320/0.5/500	323/3	Sodium	12
Sb nanosheets	etching Li−Sb alloys at H_2O-EtOH solution	620/0.1/100	212/6.4	Sodium	13
$Sb_2O_3/Ti_3C_2T_x$	solution-phase method	472/0.1/100	295/2	Sodium	14
Sb/ Sb_2O_3 nanocomposite	air oxidization	540/0.66/180	412/10	Sodium	15
Coral-like Sb_2O_3@Sb	etching & air oxidization	526.2/1/150	497.3/3	Sodium	16
Sb_2Se_3@NC@rGO	solvothermal & encapsulation method	250/0.5/350	130/1	Potassium	17
Sb_2MoO_6/rGO	hydrothermal method	247/0.5/100	161/1	Potassium	18
Sb@CNFs	electro spinning strategy	227/1/1000	121/1	Potassium	19
3DNP-Sb	vacuum-distillation method	510/0.1/50	265/0.5	Potassium	9

DFT evaluation

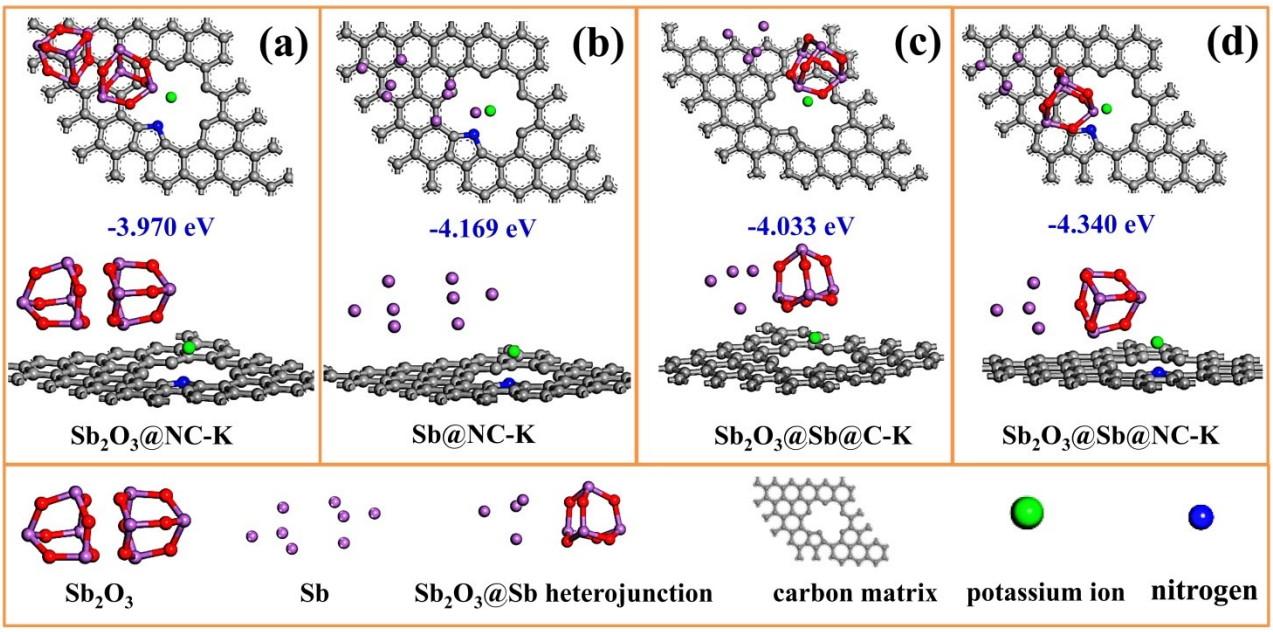

Fig. S23 Theoretical simulations and adsorption energy of (a-d) the Sb_2O_3@NC, Sb@NC Sb_2O_3@Sb@C, and Sb_2O_3@Sb@NC models for K^+.

For the PIBs, the Sb_2O_3@NC-K and Sb@NC-K possess the adsorption energies of -3.970 eV and -4.169 (**Fig. S23a-b**), whereas Sb_2O_3@Sb@NC-K (**Fig. S23d**) show the lower adsorption energy of -4.340 eV than that of Sb_2O_3@NC-K and Sb@NC-K. Obviously, the models of Sb_2O_3@Sb@C-K with Sb_2O_3@Sb@NC-K own the adsorption energies of -4.033 eV *vs* -4.340 eV (**Fig. S23c-d**), showing the positive influence of N doping for potassium storage. The relatively inferior K^+ adsorption energy intervened by Sb_2O_3@Sb heterojunction and N doping is highly believed to ensure the excellent potassium storage. These theoretical analysis results were well consistent with the displaying electrochemical performance of Sb_2O_3@Sb@NC than that of Sb_2O_3@NC, Sb@NC and Sb_2O_3@Sb@C for PIBs. According to the above discuss of DFT theory, the synergistic effect of Sb_2O_3@Sb heterojunction and N doping could effectively improve strong adsorption ability of Na^+ and K^+, leading to the enhanced sodium and potassium storage performance at high current cycling process.

References

1. Y. Zhang, P. X. Wang, Y. Y. Yin, N. N. Liu, N. Song, L. S. Fan, N. Q. Zhang and K. N. Sun, *Carbon*, 2019, **150**, 378-387.
2. P. Ge, S. Li, L. Xu, K. Zou, X. Gao, X. Cao, G. Zou, H. Hou and X. Ji, *Advanced Energy Materials*, 2019, **9**, 1803035.
3. Z. Yi, D. Fang, W. Zhang, J. Tian, S. Chen, J. Liang, N. Lin and Y. Qian, *CCS Chemistry*, 2020, **2**, 1306-1315.
4. Y. An, Y. Tian, L. Ci, S. Xiong, J. Feng and Y. Qian, *ACS nano*, 2018, **12**, 12932-12940.
5. X. Wu, Y. Chen, Z. Xing, C. W. K. Lam, S. S. Pang, W. Zhang and Z. Ju, *Advanced Energy Materials*, 2019, **9**, 1900343.
6. N. Cheng, J. G. Zhao, L. Fan, Z. M. Liu, S. H. Chen, H. B. Ding, X. Z. Yu, Z. G. Liu and B. G. Lu, *Chem Commun*, 2019, **55**, 12511-12514.
7. J. Li, N. Zhuang, J. Xie, X. Li, W. Zhuo, H. Wang, J. B. Na, X. Li, Y. Yamauchi and W. Mai, *Advanced Energy Materials*, 2019, **10**, 1903455.
8. X. Ge, S. Liu, M. Qiao, Y. Du, Y. Li, J. Bao and X. Zhou, *Angewandte Chemie*, 2019, **58**, 14578-14583.
9. T. Wu, C. Zhang, H. Hou, P. Ge, G. Zou, W. Xu, S. Li, Z. Huang, T. Guo, M. Jing and X. Ji, *Advanced Functional Materials*, 2018, **28**, 1705744.
10. A. Mahmood, S. Li, Z. Ali, H. Tabassum, B. Zhu, Z. Liang, W. Meng, W. Aftab, W. Guo, H. Zhang, M. Yousaf, S. Gao, R. Zou and Y. Zhao, *Advanced materials*, 2019, **31**, 1805430.
11. M. Kong, Y. Liu, B. Zhou, K. X. Yang, J. F. Tang, P. Zhang and W. H. Zhang, *Small*, 2020, DOI: Artn 2001976, 2001976.
12. J.-S. Park and Y. C. Kang, *Chemical Engineering Journal*, 2019, **373**, 227-237.
13. H. Li, K. Wang, M. Zhou, W. Li, H. Tao, R. Wang, S. Cheng and K. Jiang, *ACS nano*, 2019, **13**, 9533-9540.
14. X. Guo, X. Q. Xie, S. Choi, Y. F. Zhao, H. Liu, C. Y. Wang, S. Chang and G. X. Wang, *Journal of Materials Chemistry A*, 2017, **5**, 12445-12452.
15. J. Pan, N. Wang, Y. Zhou, X. Yang, W. Zhou, Y. Qian and J. Yang, *Nano Research*, 2017, **10**, 1794-1803.

16. J. Ye, G. Xia, Z. Zheng and C. Hu, *International Journal of Hydrogen Energy*, 2020, **45**, 9969-9978.

17. S. Wang, P. Xiong, X. Guo, J. Zhang, X. Gao, F. Zhang, X. Tang, P. H. L. Notten and G. Wang, *Advanced Functional Materials*, 2020, **30**, 2001588.

18. J. Wang, B. Wang, Z. Liu, L. Fan, Q. Zhang, H. Ding, L. Wang, H. Yang, X. Yu and B. Lu, *Adv Sci* 2019, **6**, 1900904.

19. H. W. Huang, J. W. Wang, X. F. Yang, R. Z. Hu, J. L. Liu, L. Zhang and M. Zhu, *Angewandte Chemie International Edition*, 2020, **59**, 14504-14510.